

Electronic supplementary information for:

Significant Power Enhancement of Magneto-Mechano-Electric Generators by Magnetic Flux Concentration

Hyunseok Song,^{‡ab} Deepak Rajaram Patil,^{‡a} Woon-Ha Yoon,^b Kwang-Ho Kim,^c Cheol Choi,^d
Jong-Hyun Kim,^e Geon-Tae Hwang,^{*f} Dae-Yong Jeong^{*g} and Jungho Ryu^{*ah}

^a School of Materials Science and Engineering, Yeungnam University, Gyeongsan 38541, Korea

^b Korea Institute of Materials Science (KIMS), Changwon, Gyeongnam, 51508, Korea

^c School of Materials Science & Engineering, Pusan National University, Busan 46241, Korea.

^d KEPCO Research Institute, Energy & Environment Laboratory, Daejeon 34056, Korea.

^e Korea Electrotechnology Research Institute (KERI), Changwon, Gyeongnam, 51543, Korea.

^f Department of Materials Science and Engineering, Pukyong National University, Busan 42601, Korea.

^g Department of Materials Science & Engineering, Inha University, Incheon 22212, Korea

^h Institute of Materials Technology, Yeungnam University, Gyeongsan 38541, Korea

[‡]These authors contributed equally to this work.

*Corresponding author: E-mail address: jhryu@ynu.ac.kr (J. Ryu), dyjeong@inha.ac.kr (D.Y.

Jeong), gthwang85@gmail.com (G. T. Hwang) Tel.: +82-53-810-2474

This file includes:

Figure S1. (a) Condition for finite element analysis (FEA) modelling of magnetic flux concentration: Magnetic field of 8 Oe is applied to MME generator and MFC in the plane direction. (b) Calculated modelling result of magnetic flux density as a function of the MFC's relative permeability. The magnetic flux density concentrated in the MME generator is saturated at the MFC's relative permeability of 600.

Figure S2. (a) FEA model of magnetic flux density distribution in the magnetostrictive layer (nickel) of the MME generator according to the different locations (L1–L4) of the MFC (area: 10 mm × 10 mm, thickness: 0.25 mm). (b) Maximum value of magnetic flux density concentrated in the MME generator by the MFC was optimized to L1.

Figure S3. (a) FEA model of the magnetic flux density distribution in the magnetostrictive layer (nickel) of the MME generator according to the different aspect ratios (A1–A5) of the MFC (area: 100 mm², thickness: 0.25 mm). (b) Maximum value of magnetic flux density concentrated in the MME generator by MFC was optimized to A5. The aspect ratios of A1, A2, A3, A4, A5 are 3:1, 2:1, 1:1, 1:2, 1:3 (width:length), respectively.

Figure S4. (a) FEA model of the magnetic flux density distribution in the magnetostrictive layer (nickel) of the MME generator according to the different shape (S1–S4) of the MFC (area: 100 mm², thickness: 0.25 mm). (b) Maximum value of the magnetic flux density concentrated in the MME generator by MFC was optimized to S2.

Figure S5. (a) i) Drawing of the optimized MFC shape for machining. ii) Optimized shape of machined MFC. (b) Max. output voltage of the MME generator under different layers of the MFC varying from 0 to 18 under a magnetic field of 8 Oe at 60 Hz. Above 10 layers, the enhancement of output voltage was minimal. Ten layers of the MFC for magnetic flux concentration to the MME generator was selected.

Figure S6. FEA result of the magnetic flux density (colour gradient) and magnetic flux distribution (white lines) inside and around the MME generator (a) without and (b) with the MFC under a magnetic field of 8 Oe.

Figure S7. The ME voltage coefficient (α_{ME}) as a function of frequency of ac magnetic field of the MME generator without magnetic proof mass. Magnetic field of 8 Oe was applied to the MME generator using a Helmholtz coil. The magnetic proof mass was removed to consider the contribution of only magnetostriction enhanced by the MFC. α_{ME} was enhanced by 141% with MFC owing to the contribution of magnetostrictive strain induced by MFC.

Figure S8. The ME voltage coefficient (α_{ME}) as a function of frequency of ac magnetic field of the MME generator with magnetic proof mass. The resonance frequency was tuned to 60 Hz by adjusting the position of proof mass. Magnetic field of 8 Oe was applied to the MME generator using a Helmholtz coil.

Figure S9. The output performance of the MME generator under magnetic field of 1 Oe at 60 Hz using a Helmholtz coil. (a) The generated open-circuit voltages from the MME generator with and without MFC. (b) The rectified (i) output dc voltages and (ii) output power of the MME generator as a function of external load resistance under 1 Oe. The peak output power of the MME generator with MFC was found to be $110 \mu W_{rms}$ which is 228% higher than that of MME generator without MFC ($50 \mu W_{rms}$).

Figure S10. Schematic of the electric circuit of the IoT system using the MME generator, harvesting power management circuit, and IoT sensor.

Figure S11. Experimental setup of the MME charging system composed of electric circuit, MME generator system, super-capacitor (0.1 F) and (d) electric circuit (100 and 1000 μ F boosted/storage capacitor and rectifier) without the MFC (a) and with the MFC (b). (c) Voltage is charged in the 0.1 F storage super-capacitor using the MME charging system for 1100 s without the MFC and for 500 s with the MFC.

Table S1. Permeability and relative permeability of materials of the MFC considered as an important parameter for magnetic flux concentration.

Table S2: Comparison of the output performance of our MME generator with that of other reported energy generators

Table S3. Operating current of the normal power consumption humidity and temperature IoT sensor on the various operating modes used for the demonstration in this study.

Other supplementary information for this manuscript

Video S1. MME operation without the MFC and with the MFC at center and optimum.

Video S2. Operation of a temperature and humidity sensor powered by MME generator using MFC.

Video S3. Comparing brightness of 100 LEDs powered by MME generator without and with MFC.

Video S4. Demonstration for operation of IoT sensor harvesting a magnetic field from power cable using MFC generating module.

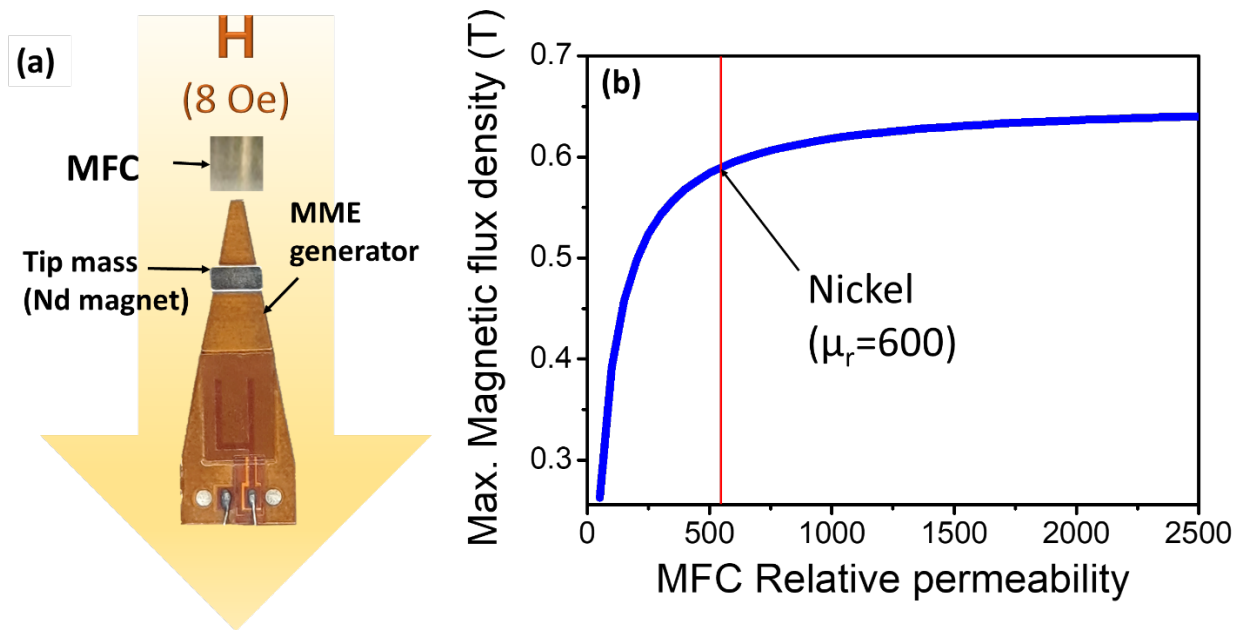


Figure S1. (a) Condition for finite element analysis (FEA) modelling of magnetic flux concentration: Magnetic field of 8 Oe is applied to MME generator and MFC in the plane direction. (b) Calculated modelling result of magnetic flux density as a function of the MFC's relative permeability. The magnetic flux density concentrated in the MME generator is saturated at the MFC's relative permeability of 600.

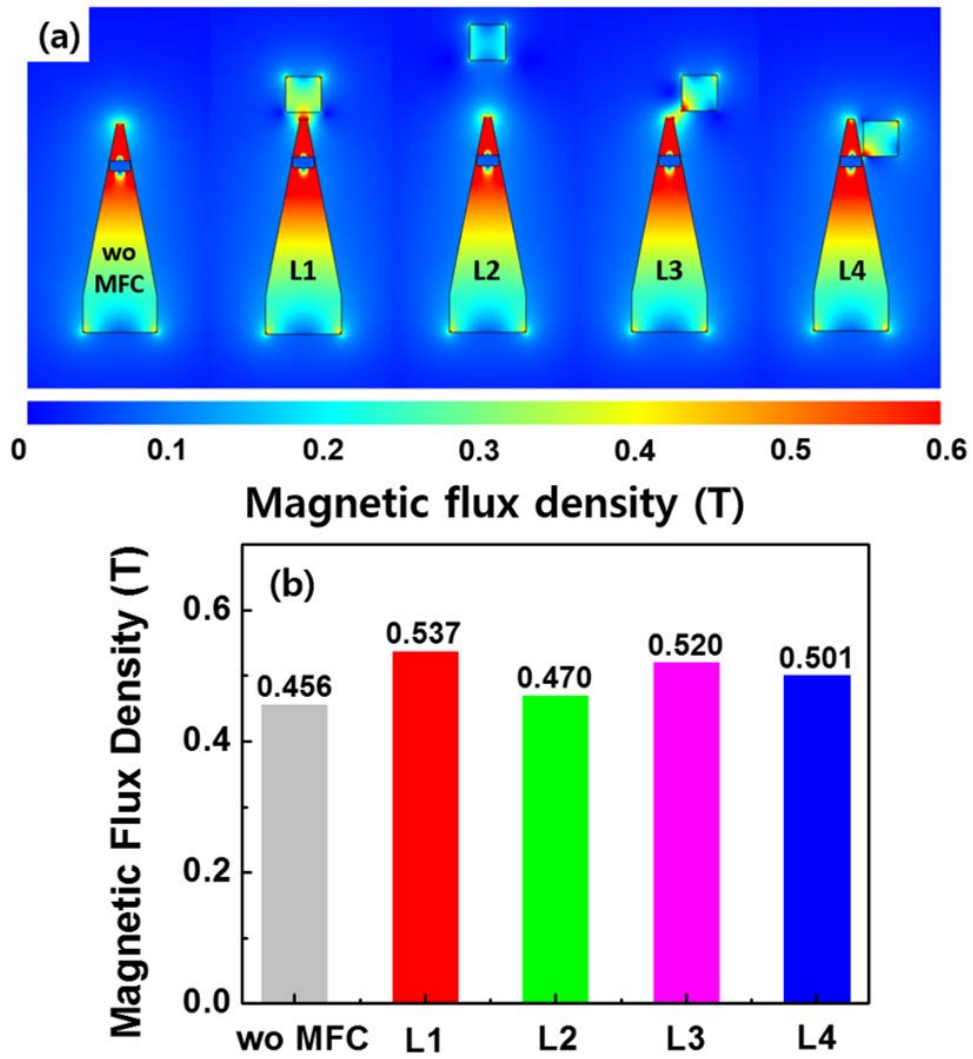


Figure S2. (a) FEA model of magnetic flux density distribution in the magnetostrictive layer (nickel) of the MME generator according to the different locations (L1–L4) of the MFC (area: $10 \text{ mm} \times 10 \text{ mm}$, thickness: 0.25 mm). (b) Maximum value of magnetic flux density concentrated in the MME generator by the MFC was optimized to L1.

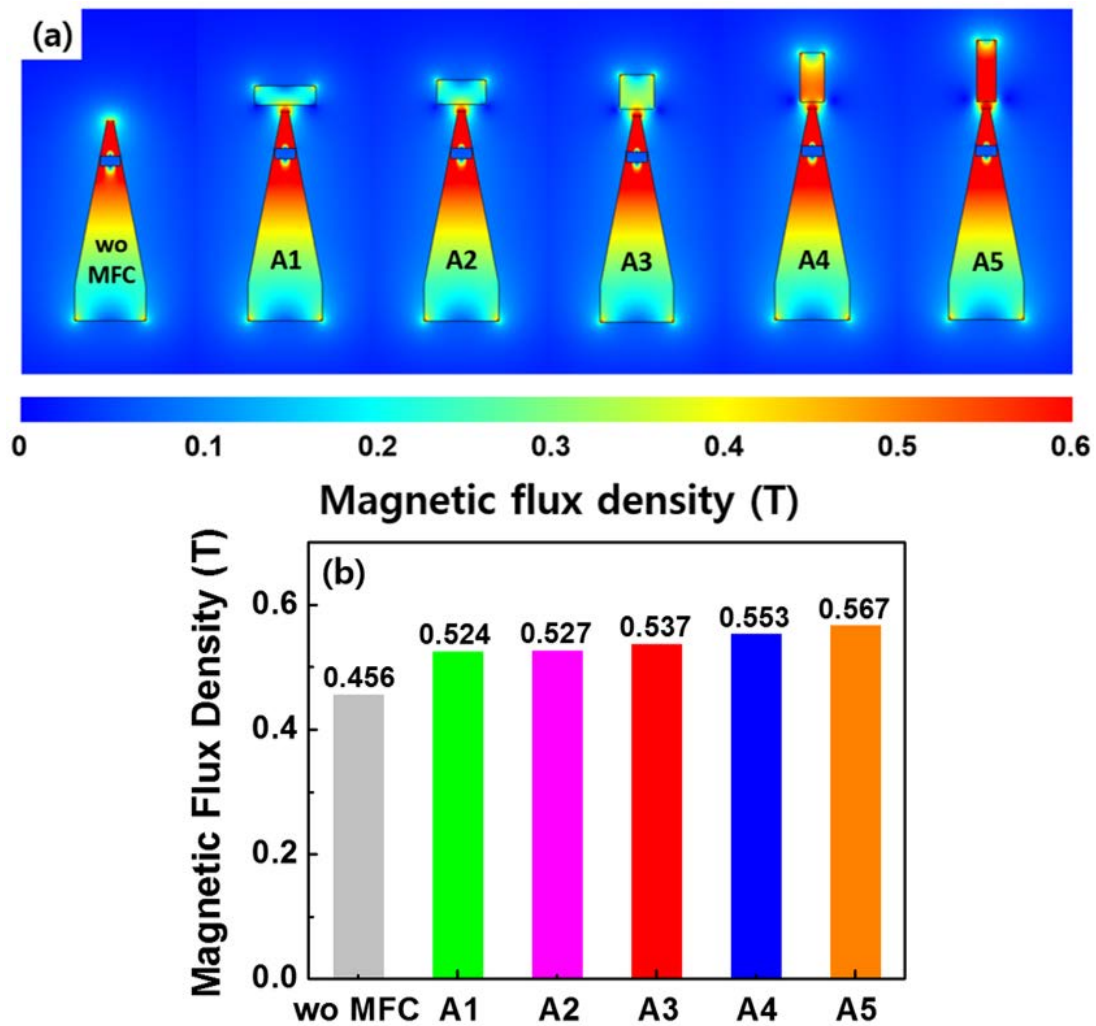


Figure S3. (a) FEA model of the magnetic flux density distribution in the magnetostrictive layer (nickel) of the MME generator according to the different aspect ratios (A1–A5) of the MFC (area: 100 mm², thickness: 0.25 mm). (b) Maximum value of magnetic flux density concentrated in the MME generator by MFC was optimized to A5. The aspect ratios of A1, A2, A3, A4, A5 are 3:1, 2:1, 1:1, 1:2, 1:3 (width:length), respectively.

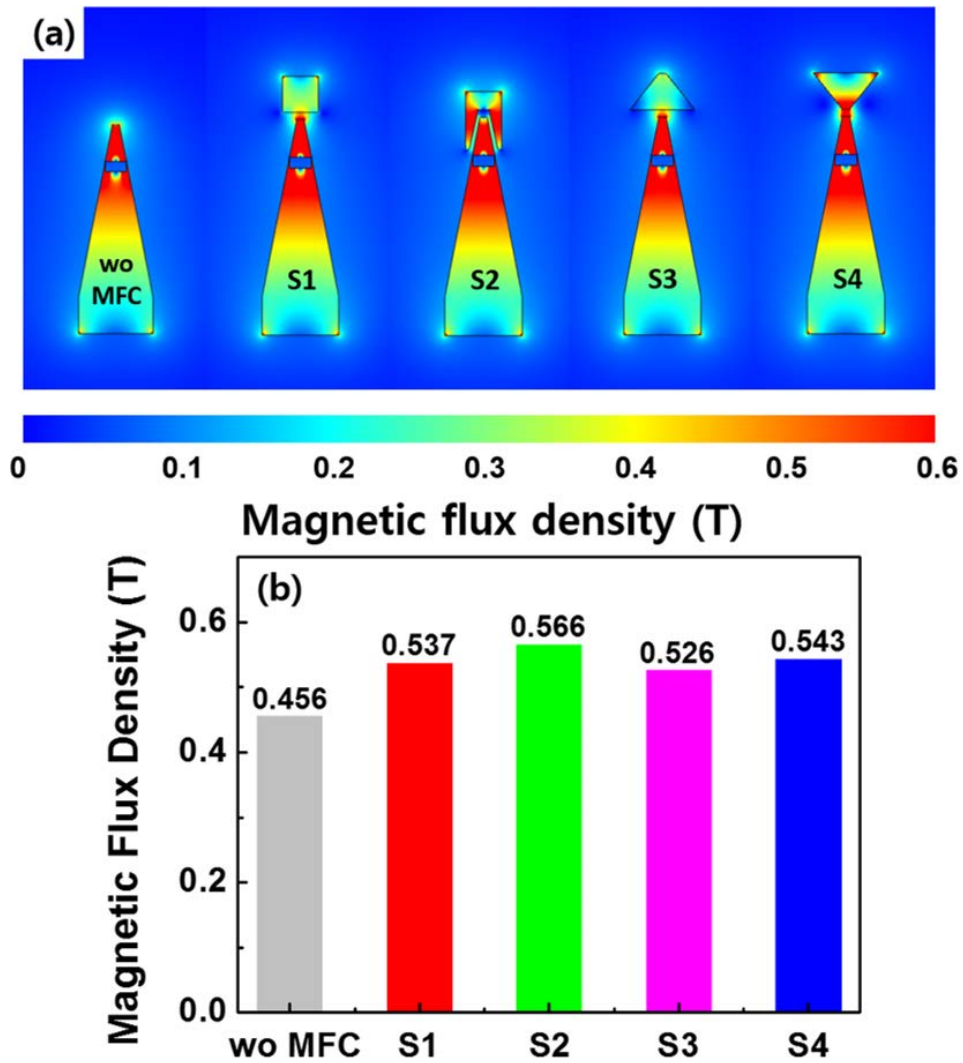


Figure S4. (a) FEA model of the magnetic flux density distribution in the magnetostrictive layer (nickel) of the MME generator according to the different shape (S1–S4) of the MFC (area: 100 mm^2 , thickness: 0.25 mm). (b) Maximum value of the magnetic flux density concentrated in the MME generator by MFC was optimized to S2.

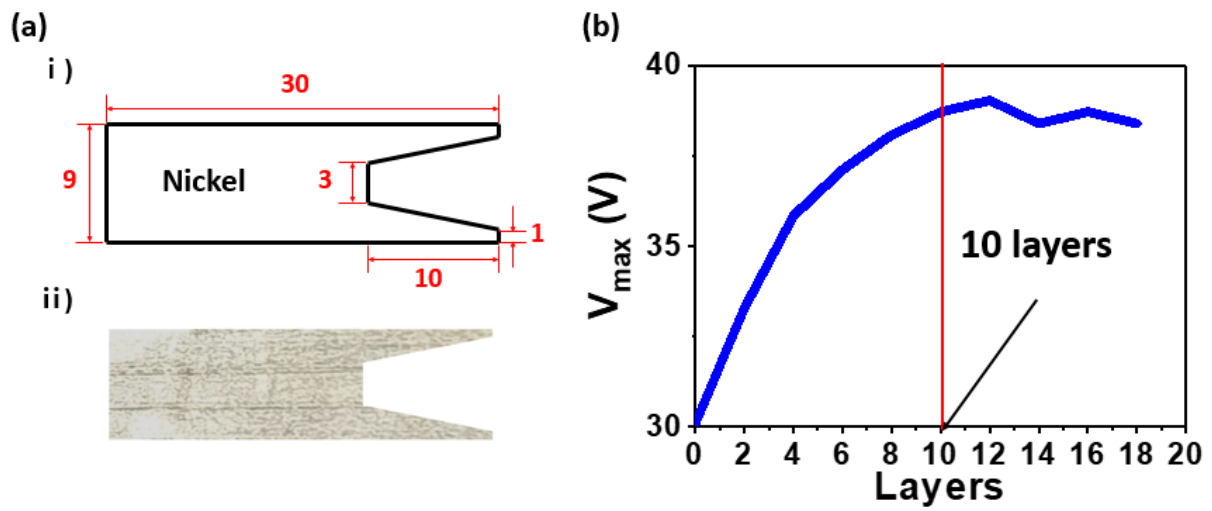


Figure S5. (a) i) Drawing of the optimized MFC shape for machining. ii) Optimized shape of machined MFC. (b) Max. output voltage of the MME generator under different layers of the MFC varying from 0 to 18 under a magnetic field of 8 Oe at 60 Hz. Above 10 layers, the enhancement of output voltage was minimal. Ten layers of the MFC for magnetic flux concentration to the MME generator was selected.

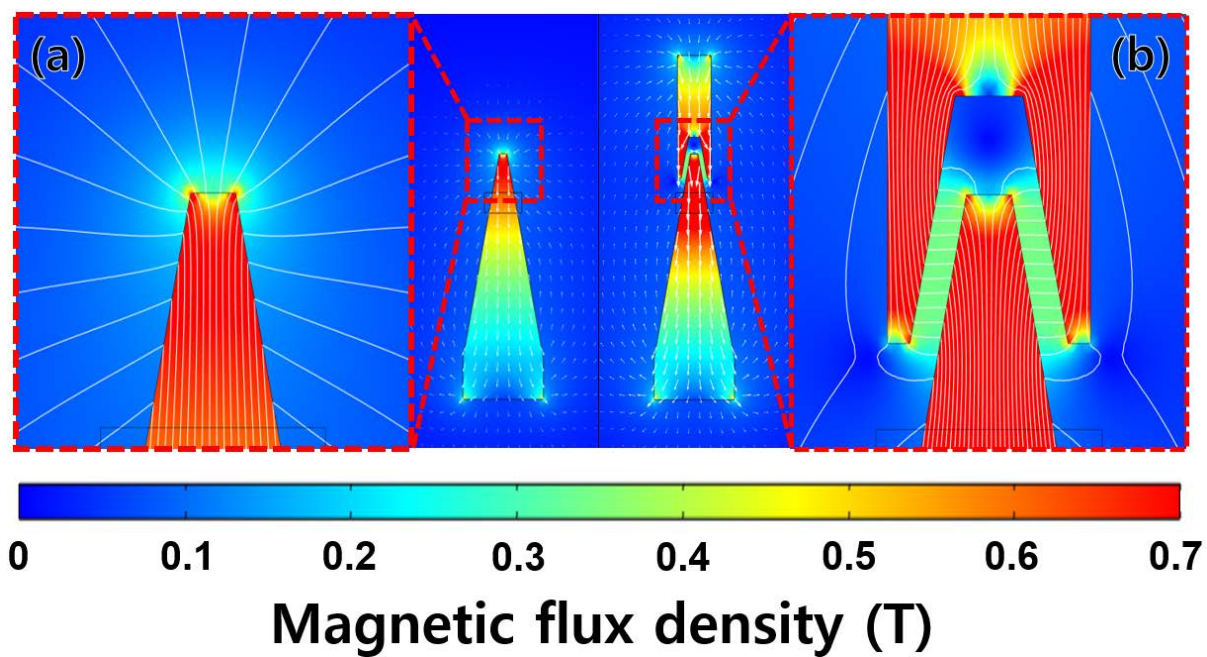


Figure S6. FEA result of the magnetic flux density (colour gradient) and magnetic flux distribution (white lines) inside and around the MME generator (a) without and (b) with the MFC under a magnetic field of 8 Oe.

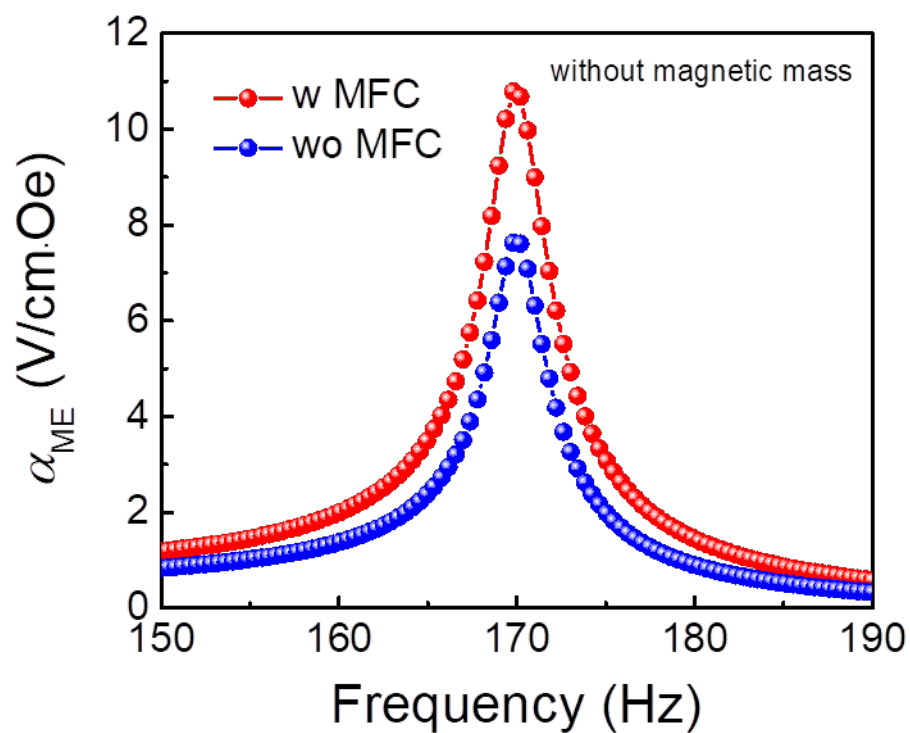


Figure S7. The ME voltage coefficient (α_{ME}) as a function of frequency of ac magnetic field of the MME generator without magnetic proof mass. Magnetic field of 8 Oe was applied to the MME generator using a Helmholtz coil. The magnetic proof mass was removed to consider the contribution of only magnetostriction enhanced by the MFC. α_{ME} was enhanced by 141% with MFC owing to the contribution of magnetostrictive strain induced by MFC.

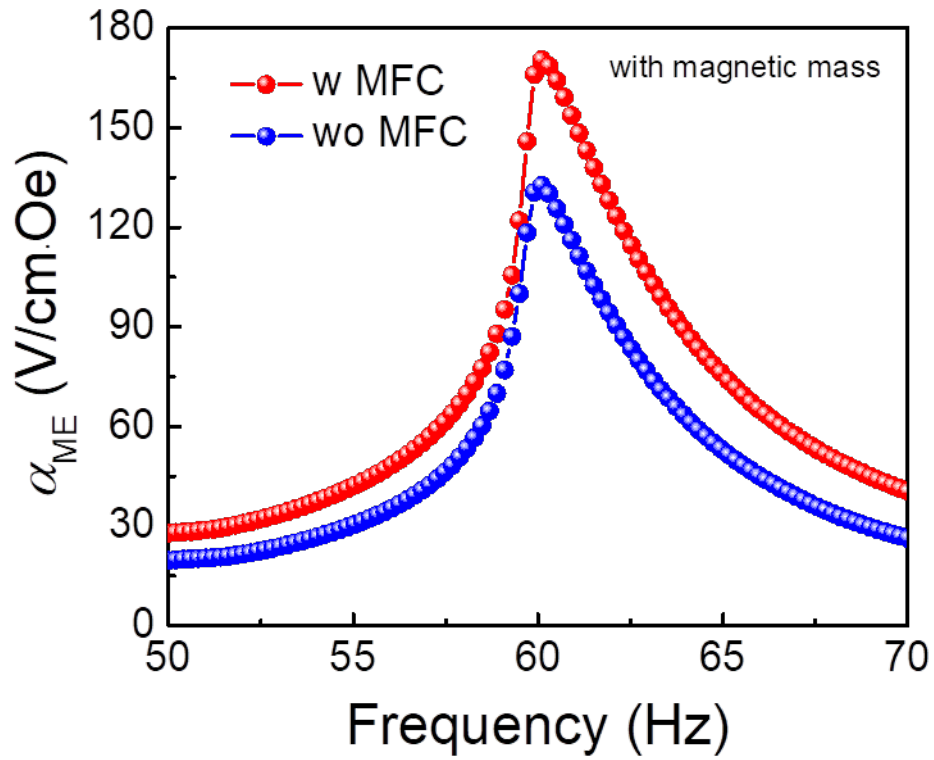


Figure S8. The ME voltage coefficient (α_{ME}) as a function of frequency of ac magnetic field of the MME generator with magnetic proof mass. The resonance frequency was tuned to 60 Hz by adjusting the position of proof mass. Magnetic field of 8 Oe was applied to the MME generator using a Helmholtz coil.

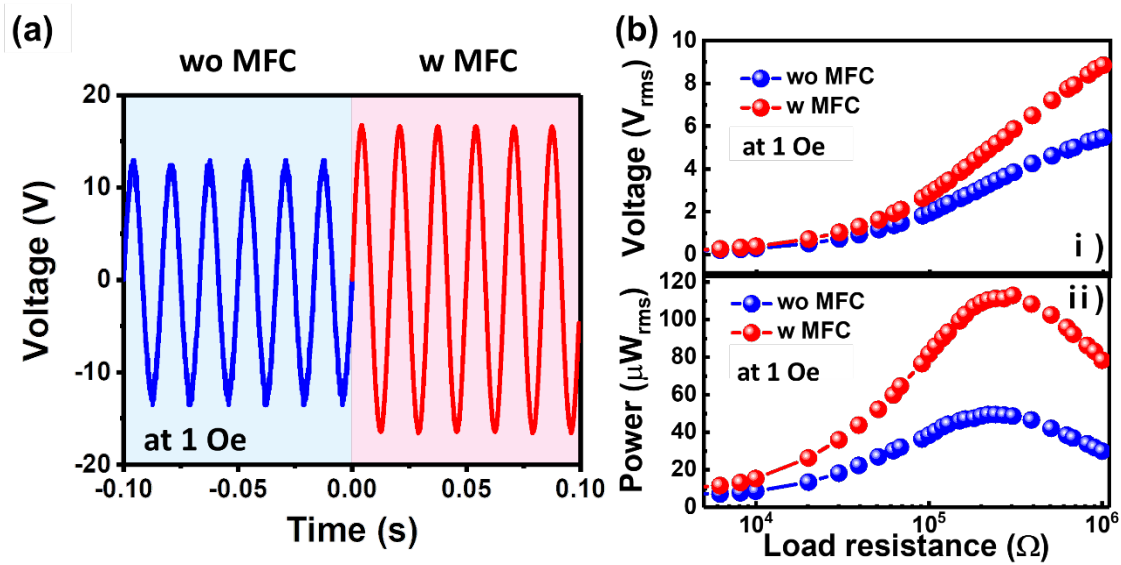


Figure S9. The output performance of the MME generator under magnetic field of 1 Oe at 60 Hz using a Helmholtz coil. (a) The generated open-circuit voltages from the MME generator with and without MFC. (b) The rectified (i) output dc voltages and (ii) output power of the MME generator as a function of external load resistance under 1 Oe. The peak output power of the MME generator with MFC was found to be 110 μW_{rms} which is 228% higher than that of MME generator without MFC (50 μW_{rms}).

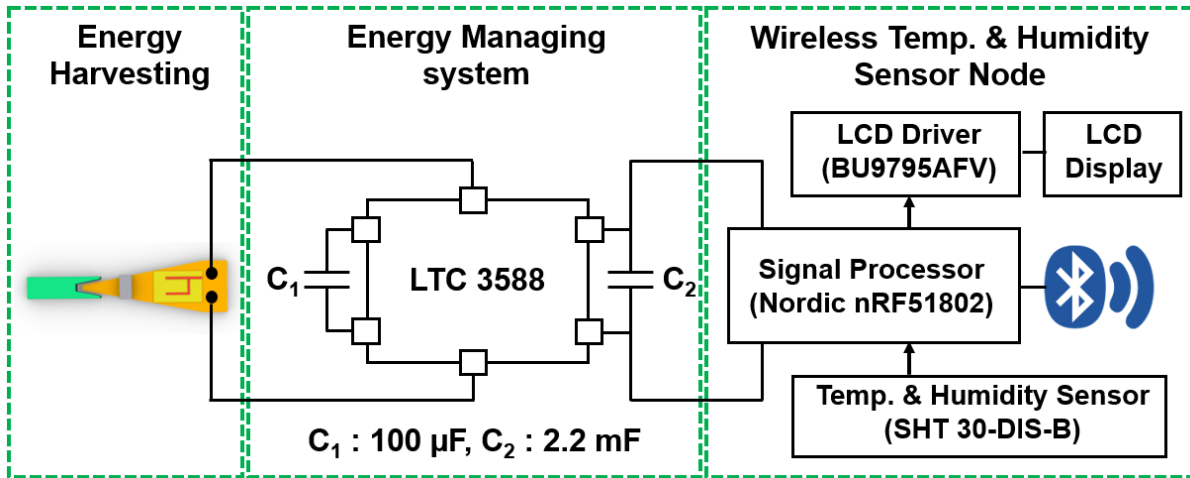


Figure S10. Schematic of the electric circuit of the IoT system using the MME generator, harvesting power management circuit, and IoT sensor.

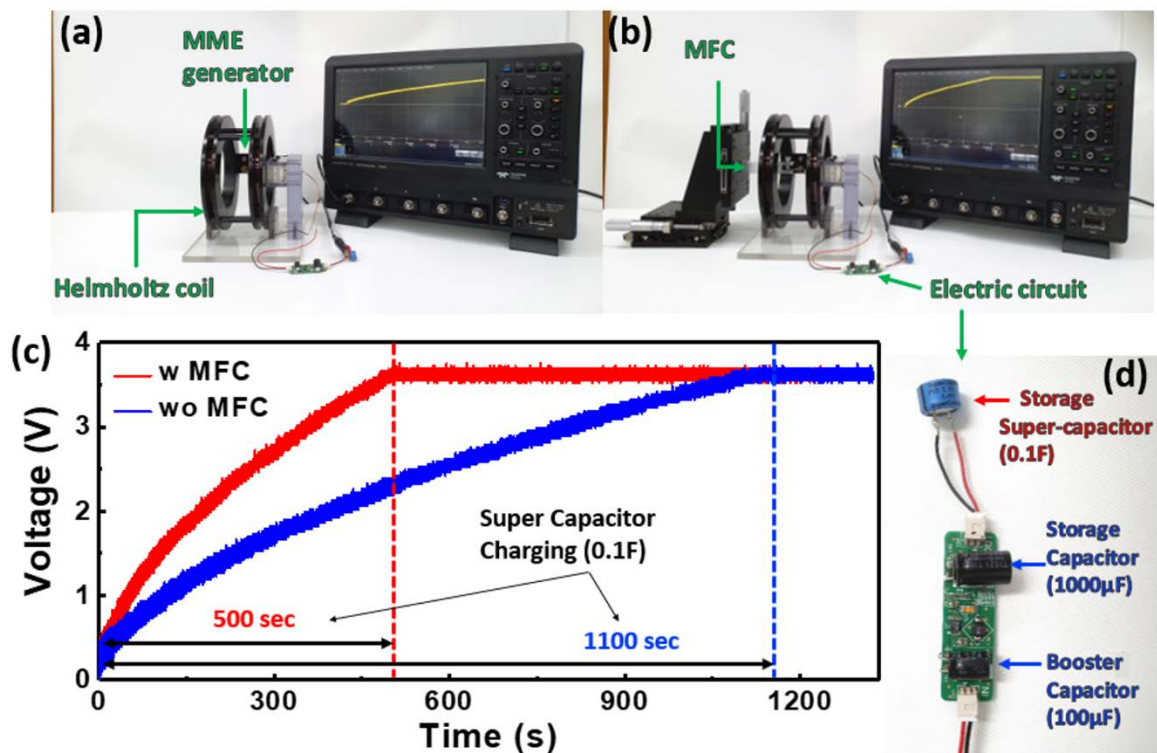


Figure S11. Experimental setup of the MME charging system composed of electric circuit, MME generator system, super-capacitor (0.1 F) and (d) electric circuit (100 and 1000 μF booster/storage capacitor and rectifier) without the MFC (a) and with the MFC (b). (c) Voltage is charged in the 0.1 F storage super-capacitor using the MME charging system for 1100 s without the MFC and for 500 s with the MFC.

Material	Permeability, μ (H/m)	Relative permeability, μ/μ_0
Metglas 2714A (annealed)	1.26×10^0	1000000
Iron (99.95% pure annealed Fe)	2.5×10^{-1}	200000
Cobalt-iron (high permeability strip material)	2.3×10^{-2}	18000
Iron (99.8% pure)	6.3×10^{-3}	5000
Ferritic stainless steel (annealed)	$1.26 \times 10^{-3} - 2.26 \times 10^{-3}$	1000 – 1800
Martensitic stainless steel (annealed)	$9.42 \times 10^{-4} - 1.19 \times 10^{-3}$	750 – 950
Carbon steel	1.26×10^{-4}	100
Nickel	$1.26 \times 10^{-4} - 7.54 \times 10^{-4}$	100 – 600
Neodymium magnet	1.32×10^{-6}	1.05
Aluminum	1.256665×10^{-6}	1.000022
Air	$1.25663753 \times 10^{-6}$	1.00000037
Vacuum	$4\pi \times 10^{-7} (\mu_0)$	1, exactly
Copper	1.256629×10^{-6}	0.999994

Table S1. Permeability and relative permeability of materials of the MFC considered as an important parameter for magnetic flux concentration.

MME generator	Active Area (cm ²)	Power (mW)	Magnetic field (Oe)	Areal Power density (mW/cm ²)	Power density (mW/cm ² Oe ²)	Reference
Ni/PMNPZT (low loss SFC)	2.8×1.4	0.7 _{dc}	7	0.18	0.004	1
Metglas/PMN-PZT (SFC)	2.8×1.4	6.93 _{rms}	10	1.76	0.0176	2
FeGa/PMNPZT (SFC)	2.8×1.4	3.86 _{dc}	7	0.98	0.020	3
Metglas/PMN-PZT (SFC)	2.8×1.4	4.5 _{rms}	10	1.14	0.011	4
Ti/PFA	5.0×2.0	4.8 _{rms}	7	0.48	0.010	5
Metglas/PZT	3.6×3.1	0.4 _{rms} 5.32 _{rms}	1 5	0.035 0.47	0.035 0.019	6
Ni/PMNPZT with MFC	2.0×1.3	3.33_{rms}	8	1.28	0.02	Present work

Table S2: Comparison of the output performance of our MME generator with that of other reported energy generators

	Model No. / Company	Operating Mode	Operating Current	Operating Power
Humidity and Temp. Sensor	SHT3x-DIS / Sensirion	Standby	0.2 μ A	0.72 μ W
		Measuring	600 μ A	2.16 mW
LCD Display	BU9795AFV / Rohm	Standby	5 μ A	18 μ W
		Run	16 μ A	57.6 μ W
Processing / Data Communication	nRF51802 / Nordic	Standby	30 μ A	108 μ W
		Run (oscillator)	540 μ A	1.94 mW
		Run (CPU)	600 μ A	2.16 mW
		Run (Radio Transceiver)	7.5 mA	27 mW

Table S3. Operating current of the normal power consumption humidity and temperature IoT sensor on the various operating modes used for the demonstration in this study.

References:

- 1.V. Annapureddy, M. Kim, H. Palneedi, H. Y. Lee, S. Y. Choi, W. H. Yoon, D. S. Park, J. J. Choi, B. D. Hahn, C. W. Ahn, J. W. Kim, D. Y. Jeong and J. Ryu, *Adv. Energy Mater.*, 2016, **6**, 1601244.
- 2.M. G. Kang, R. Sriramdas, H. Lee, J. Chun, D. Maurya, G. T. Hwang, J. Ryu and S. Priya, *Adv. Energy Mater.*, 2018, **8**, 1703313.
- 3.V. Annapureddy, S. M. Na, G. T. Hwang, M. G. Kang, R. Sriramdas, H. Palneedi, W. H. Yoon, B. D. Hahn, J. W. Kim, C. W. Ahn, D. S. Park, J. J. Choi, D. Y. Jeong, A. B. Flatau, M. Peddigari, S. Priya, K. H. Kim and J. Ryu, *Energy Environ. Sci.*, 2018, **11**, 818–829.
- 4.R. Sriramdas, M. G. Kang, M. Meng, M. Kiani, J. Ryu, M. Sanghadasa and S. Priya, *Adv. Energy Mater.*, 2020, **10**, 1903689.
- 5.K. W. Lim, M. Peddigari, C. H. Park, H. Y. Lee, Y. Min, J. W. Kim, C. W. Ahn, J. J. Choi, B. D. Hahn, J. H. Choi, D. S. Park, J. K. Hong, J. T. Yeom, W. H. Yoon, J. Ryu, S. N. Yi and G. T. Hwang, *Energy Environ. Sci.*, 2019, **12**, 666–674.
6. H. Lee, R. Sriramdas, P. Kumar, M. Sanghadasa, M. G. Kang, S. Priya, *Energy Environ. Sci.*, 2020, **13**, 1462-1472